Impact-driven oxidation of organics explains chondrite shock metamorphism dichotomy

Kurosawa, Kosuke ; Collins, Gareth S. ; Davison, Thomas M. ; Okamoto, Takaya ; Ishibashi, Ko ; Matsui, Takafumi

(Citation)
Nature Communications,16(1):3608

(Issue Date)
2025-04-24

(Resource Type)
journal article

(Version)
Version of Record

nature communications

Article https://doi.org/10.1038/s41467-025-58474-2

Impact-driven oxidation of organics explains chondrite shock metamorphism dichotomy

Received: 10 July 2024

Accepted: 24 March 2025

Published online: 24 April 2025

Check for updates

Kosuke Kurosawa [1,2] ✉, Gareth S. Collins [3], Thomas M. Davison [3], Takaya Okamoto [2], Ko Ishibashi [2] & Takafumi Matsui [2,4,5]

Shocked meteorites can be used to probe the dynamics of the early Solar system. Carbonaceous chondrites are less shocked than ordinary chondrites, regardless of the degree of aqueous alteration. Here, we show that this shock metamorphic dichotomy is a consequence of impact-driven oxidation of organics that are abundant in carbonaceous but not ordinary chondrites. Impact experiments at 3–7 km s^{-1} using analogs of chondrite matrices reveal evidence of local heating in the matrix up to ~2000 K. Impacts on carbonaceous asteroids cause explosive release of CO and/or CO_2, which can efficiently remove evidence of shock. We show that highly shocked materials are lost to space from typical-sized chondrite parent bodies (~100 km in diameter), but are retained on the largest known carbonaceous asteroid, namely, (1) Ceres, due to its stronger gravity. Ceres' surface is thus a witness plate for the ancient impact environment of carbonaceous chondrite parent bodies.

Shocked meteorites are Rosetta stones to decode the dynamical environment in the early Solar system[1] because a single impact event produces a variety of shock metamorphism in different minerals[2]. Progressive shock stages have been constructed[2,3] to classify shocked meteorites[3,4]. Figure 1 shows the number fraction of ordinary (NC)[4] and carbonaceous (CC) chondrites[3] as a function of shock degree. There is a clear dichotomy between NCs and CCs in terms of shock metamorphism. The fraction of highly shocked CCs ranked ≥S3 (>15 GPa) is only ~15%, whereas ≥63% of NCs are classified into ≥S3. Samples returned from carbonaceous asteroid Ryugu did not contain obvious shocked features[5], except for a micro fault[6,7], a high-pressure mineral[6], and small crystallographic misorientations in an olivine grain[8]. Since the shock pressure on Ryugu was estimated to be 2–10 GPa[6–8], Ryugu samples were classified as S1–S2 (≤10 GPa). Impact-induced dehydration of phyllosilicates has been proposed qualitatively as a mechanism to explain the virtually unshocked nature of hydrous CCs including CI and CM chondrites[9]; however, anhydrous CCs, such as CO and CV types, are also less shocked than NCs. In addition, a recent reevaluation of dehydration from phyllosilicates during impacts demonstrated that water vapor production is much lower than previously expected[10].

It has been known that ~80% of meteorites, including NCs and CCs, come from a small number of parent bodies that have young asteroid families[11–15]. These asteroid families were formed due to catastrophic disruption recently (10–1000 Ma) with respect to the age of the Sun[11,12] and their associated meteorites were likely launched from the families at 1–100 Ma by impact events[16]. Consequently, the parent bodies are expected to witness impact bombardments for up to ~4.5 Gyrs. For example, the Chelyabinsk meteorite recorded at least eight impact events[17]. Despite the limited number of parent bodies, shocked meteorites provide a rich record of impact.

The straightforward interpretation of the less-shocked nature of CCs is that impact velocities on the parent bodies of CCs were lower than on those of NCs. It is widely known that an isotopic dichotomy between NCs and CCs exists on a $\varepsilon^{54}Cr$–$\varepsilon^{50}Ti$ diagram[18] and hence that the birth places of NC and CC parent bodies were spatially divided in the early solar nebula[19]. According to this model, the parent bodies of CCs form beyond the orbit of the proto-Jupiter while those of NCs form in the inner Solar System. Since the impact velocity distribution is expected to be proportional to the Keplerian velocity v_K around the Sun ($v_K \propto a^{-1/2}$, where a is the semi-major axis), impact velocities onto

[1]Department of Human Environmental Science, Graduate School of Human Development and Environment, Kobe University, Nada-ku, Kobe, Hyogo, Japan. [2]Planetary Exploration Research Center, Chiba Institute of Technology, Narashino, Chiba, Japan. [3]Impact and Astromaterials Research Centre, Department of Earth Science and Engineering, Imperial College London, London, UK. [4]Institute for Geo-Cosmology, Chiba Institute of Technology, Narashino, Chiba, Japan. [5]Deceased: Takafumi Matsui. ✉e-mail: kosuke.kurosawa@people.kobe-u.ac.jp

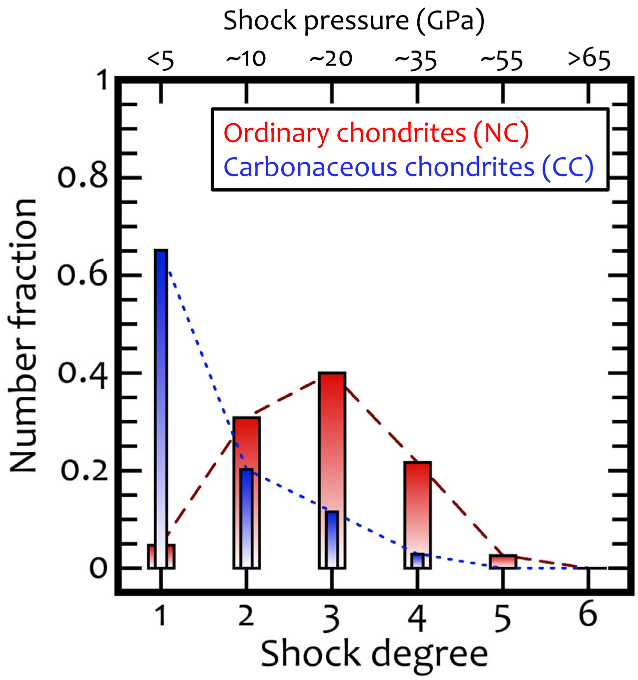

Fig. 1 | Shock metamorphic dichotomy in chondrites. The number fraction of ordinary (NC, red thick) and carbonaceous (CC, blue thin) chondrites as a function of shock degree. The data are taken from the previous studies[3,4]. The corresponding approximate shock pressure of each shock degree is also shown on the top *x*-axis.

the CC parent bodies could be as low as ~1 km s^{-1} in the Kuiper Belt Object (KBO) region[20,21] compared with the typical impact velocity of ~5 km s^{-1} in the main belt[22]. This scenario seems to be consistent with the shock metamorphic dichotomy. However, the parent bodies of CCs must migrate from their original orbit (>5 AU) to the Main Belt Asteroid (MBA) region (2–5 AU) at some stage[23]. The most plausible driving force of such migration is gravitational scattering during the early orbital instability of the gas giants, including Jupiter, Saturn, Uranus, and Neptune[24–26]. Moreover, the strong remanent magnetization of Ryugu particles[5] suggests that the parent body of carbonaceous asteroid Ryugu was injected into the MBA region before the dissipation of the solar nebula, that is, within several Myrs after the formation of the Sun[27]. If most CC parent bodies also migrated at this time, the parent bodies of both NCs and CCs must have spent ~4.5 Gyr in the MBA region under strong gravitational perturbation from Jupiter. Consequently, the sample evidence from Ryugu and recent dynamical theories imply that the impact conditions of NC and CC parent bodies were likely similar to each other during past 4.5 Gyrs.

Here, we propose a hypothesis that the shock metamorphic dichotomy is a consequence of the difference in response to impact shock between NC and CC parent bodies rather than different impact conditions for NC and CC bodies. Since CC bodies contain abundant organics in their matrices, the mechanical and thermochemical properties of CC materials differ substantially from those of NC materials. We conducted impact experiments with analog materials of chondrite matrices to investigate the effects of organics on the samples' response to impact. The impact velocity v_{imp} was varied from 3 to 7 km s^{-1}, which spans the typical v_{imp} in the main asteroid belt[22]. The methodology is summarized in the Methods section.

Results

Roles of carbon in shock-induced devolatilization

Our impact experiments used four porous target pellets, named Fe–O, Fe–O–C, Si–O, and Si–O–C. We used commercial powder reagents of magnetite (Fe_3O_4), quartz (SiO_2), and graphite to make analogs of the chondrite matrices of aqueous-altered and anhydrous carbonaceous chondrites. We simplified the target compositions to clearly isolate the effects of the presence of the carbon on the total vapor production. The other reasons for our choice of powders and the justification for the choice in detail are described in the Methods section. The porosity of the pellets was adjusted to ~60%, which is close to the typical value of the chondrite matrices[28], except for a few cases to investigate the effects of porosity on the outcomes (Supplementary Note, S1 and Fig. S1). The atomic ratio of C to O for the target was set to 0.1, which is close to the C/O ratio of CI chondrites[29] as a fiducial case. The corresponding carbon content f_{C} of the Fe–O–C and Si–O–C targets was 2 wt.% and 4 wt.%, respectively. Since the carbon content of the Si–O–C targets, which are analogs of the matrices of CO and CV chondrites, was higher than the actual chondritic value, we investigated the effects of carbon content of the Si–O–C targets on the impact outcomes (Supplementary Note, S2). We confirmed that the dependence of the total production of CO and CO_2 on f_{C} was not significant in the case where the targets contain carbon down to 0.3 wt.% of f_{C}. The total vapor production is proportional to $f_{\mathrm{C}}^{0.6}$ (Supplementary Fig. S2). In this sensitivity test, we also used ^{13}C amorphous carbon for the Si–O–C targets to increase the signal-to-noise ratio in mass spectrometry especially at relatively low impact velocities. Figure 2 shows the results of the mass spectrometry at an impact velocity v_{imp} of 4.2–4.8 km s^{-1}. This impact velocity is close to the typical impact velocity in the main asteroid belt[22]. Hereafter, we denote the ion current for the mass number $M/Z = i$ as I_i. We clearly detected a rise in all or some of $I_{28}(CO^+)$, $I_{32}(O_2^+)$, and $I_{44}(CO_2^+)$ from the targets except for the Si–O target, showing that the vaporization of magnetite and quartz and/or the oxidation of the organics occurs. Although vaporization of the Si–O target was not detected at $v_{\mathrm{imp}} = 4.5$ km s^{-1}, a rise in I_{32} for the Si–O target was observed at velocities higher than 5.8 km s^{-1}. Since the experimental chamber was buffered by an argon gas flow up to 500 Pa to minimize chemical contamination by the gases inevitably produced by the gun operation[30], the ion current ratio of I_i to $I_{40}(Ar^+)$ corresponds to the partial pressure of the gas species having $M/Z = i$ in the experimental chamber. Although the I_{40} level was slightly different from shot-to-shot, it was stable during the measurements even at the time of the impact ($t = 0$ s, where t is the time after impact). We can quantify the total production of CO, O_2 and CO_2 based on the ion current ratios. The procedures for the calibration of the measuring system and data reduction are described in detail in the Supplementary Information (Supplementary Note S3 and Figs. S3 and S4). Figure 3 shows the total vapor production M_{vap} as a function of impact velocity. The sum of the masses of CO, O_2, and CO_2 at each shot is shown here. The comparison of M_{vap} between Fe–O and Fe–O–C, and Si–O and Si–O–C, shows the presence or absence of carbon greatly affects the total vapor production, and the presence of carbon substantially enhances the degree of vaporization of the matrix minerals up to two orders of magnitude. The gas production of each gas can be found in Supplementary Note, S4 and Fig. S5. The effects of the incidence angle of projectiles onto the target on the total vapor production should be noted. It is widely known that all natural impacts occur at an oblique incidence angle[31], while here we only performed vertical impacts. According to oblique impact experiments[32], the heat generated during an impact is the sum of shock heating and subsequent shear heating. The heat generated due to the former and latter mechanisms exhibits an inverse correlation with impact angle at least down to 15 degrees measured from the horizontal[32]. The enhancement of shear heating in a more oblique impact tends to compensate for the weaker shock heating. Consequently, we suggest that the total gas production shown in Fig. 3 is a first-order estimation in the case of oblique impacts.

Discussion

Evidence for local high temperature

The impact experiments reveal that local energy concentration occurs in the porous targets in cases both with and without carbon. First, we

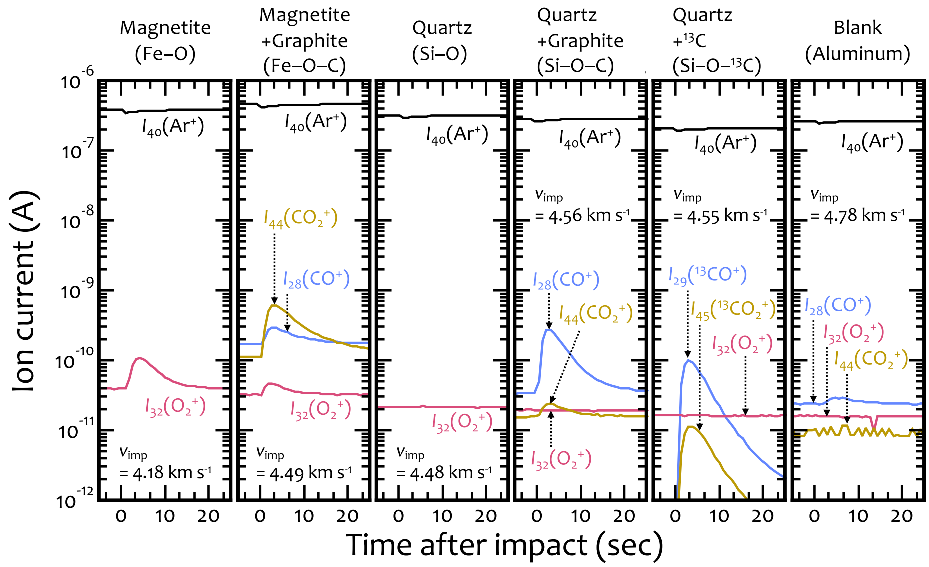

Fig. 2 | Mass spectrometry data. Time variation of the ion currents for gases with the mass numbers I_i. The target compositions are shown on the top of the panels. The impact velocities υ_{imp} of the shots (indicated in the panels) were similar. Also shown are results with ^{13}C amorphous carbon (Si–O–^{13}C) and a blank experiment using an aluminum plate for comparison. The carbon content of the Si–O–^{13}C target was 1.6 wt.%, which is 40% of the Si–O–C target (See Supplementary Note S2).

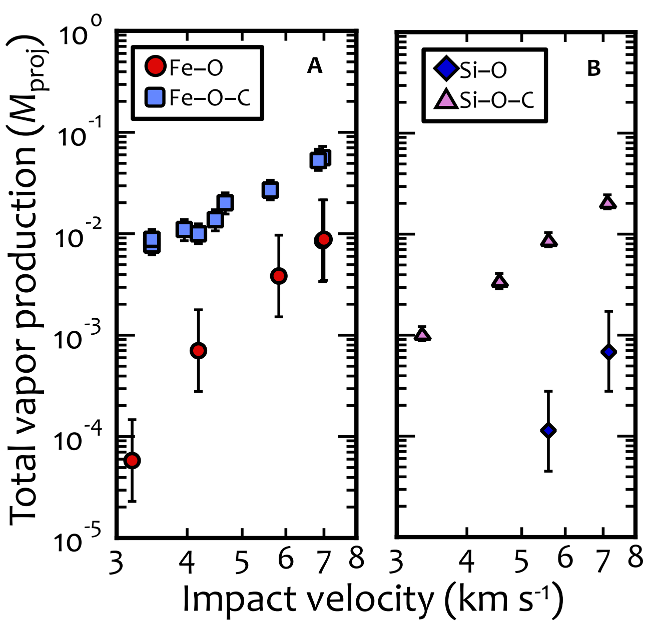

Fig. 3 | The enhancement of the total vapor production due to the presence of carbon. The total vapor production normalized by the projectile mass as a function of impact velocity for hydrous (**A**) and anhydrous (**B**) chondrite analogs. Vapor production from the Si–O target was not detected at impact velocities lower than 5.8 km s^{-1}. The atomic ratio of carbon to oxygen for the targets with carbon was 0.1 (See text). The error bars are come from the fitting errors in the calibration experiments (Supplementary Note S3 and Supplementary Fig. S4).

discuss the C-free targets, that is, Fe–O and Si–O. We conducted shock physics and thermochemical modeling to investigate the degree of heating in the porous magnetite (Fe–O) and quartz (Si–O) targets. As equations of state were available or could be easily constructed for these single-mineral materials, we calculated the mass, momentum, and energy transfer from the impact point to the inside of the target with the iSALE shock physics code[33–36]. Since the matrix particle size of 1–10 µm is much smaller than the projectile diameter of 2 mm, we treated the targets as continuous microporous media with uniform initial porosity in the shock physics code. Further details are described in the Methods section (See also Supplementary Notes, S5 and, S6, Supplementary Fig. S6, and Supplementary Table, S1).

Figure 4 shows a comparison of the decomposed target mass between the experimental and numerical results. We found that the actual decomposed mass in the experiments is only 5–40% of the numerical predictions. In contrast, we detected the decomposition of quartz and magnetite in the experiments at a velocity where decomposition does not occur in the modeling. We attribute both differences to localized concentrations of heat caused by a non-uniform distribution of porosity. Our simulations assume uniform initial porosity and hence a uniform degree of pore crushing and shock heating. Local variations in porosity in the real samples would create zones hotter and cooler than the average as demonstrated by shock physics modeling at the meso-scale[28,37], which would lower the bulk threshold of the onset of incipient devolatilization and shield some of the sample from decomposing.

Second, we discuss our results for the targets with carbon, which are Fe–O–C and Si–O–C. In this case, the absence of available equation of state models precluded investigation by shock physics simulations. Instead, the measured molar ratio of CO to CO_2 can be used as a thermometer because it is controlled solely by the temperature-dependent oxygen fugacity[10]. We obtained theoretical curves of temperature versus CO/CO_2 ratio for the Fe–O–C and Si–O–C targets with the NASA CEA code[38]. Figure 5A shows the measured CO/CO_2 ratio as a function of impact velocity. The CO/CO_2 ratio pertaining to the Fe–O–C targets increases as υ_{imp} increases and the CO/CO_2 ratio for the Si–O–C targets is nearly constant. Figure 5B shows the predicted CO/CO_2 ratio as a function of temperature assuming thermal equilibrium. We can estimate the temperatures at the locations where the oxidation of carbon occurred by comparing the observed CO/CO_2 ratios in the experiments with the thermochemical model curves. We found that the temperature of the reaction field exceeds 2000 K even at υ_{imp} ~ 4 km s^{-1}. Further results of the thermochemical calculations are described in Supplementary Note S5. The implied gas temperature is much higher than the temperature required for decomposition of magnetite and quartz under the condition where carbon coexists (See Supplementary Fig. S6). The unexpected high temperature is further evidence for localization of heat in the porous target. The energy localization results in a heterogeneous distribution of temperature

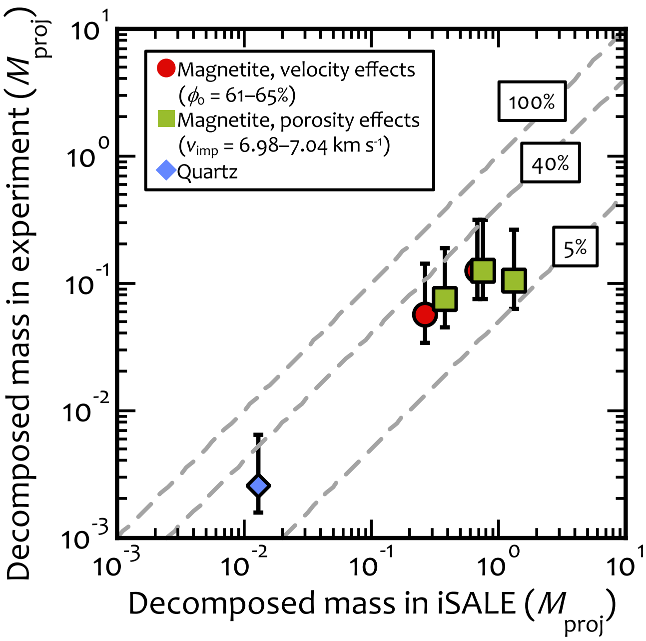

Fig. 4 | Comparison between the experimental and numerical results. The red circles show the results for impact velocities from 3.2 to 7.0 km s^{-1}. The green squares include data where porosity ranged from 51% to 79%. The error bars on the experimental data have come from the fitting errors in the calibration experiments as well as Fig. 3. The gray dashed lines show 5%, 40% and 100% of the numerical results.

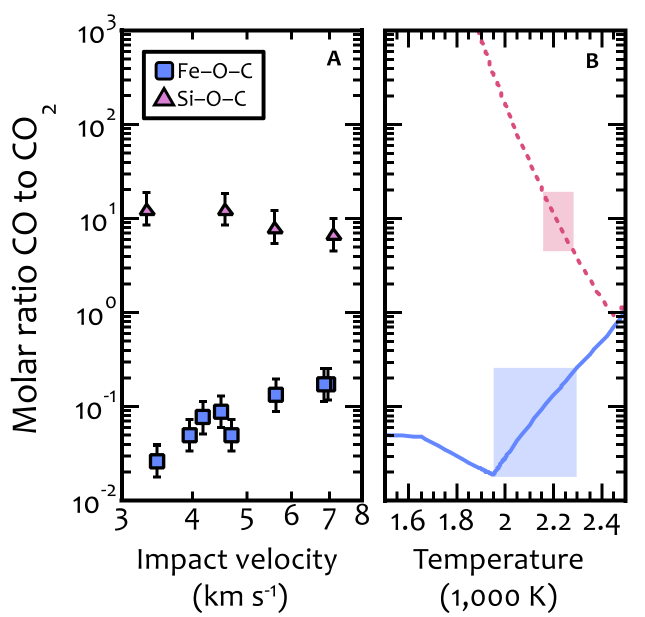

Fig. 5 | Gas temperature estimation. A shows the molar ratio of CO to CO_2 measured in the experiments as a function of impact velocity. The error bars are the uncertainties in the molar ratio due to the error propagation from the CO and CO_2 productions. **B** shows the equilibrium composition of the molar ratio as a function of temperature. In this calculation, the elemental abundances were set to the same as the targets. The shaded regions correspond to the experimental results.

during shocks in chondrite matrices, which is consistent with the observation of a polished thin section of CR2 chondrite GRA 06100[28].

Explosive dispersal makes an "apparent" dichotomy in shock metamorphism

Here, we discuss the sequence of events after hypervelocity impact on a carbonaceous asteroid. Local heating of the matrix is expected to cause the generation of CO and CO_2 with the temperatures above 2000 K at least in the velocity range performed in this study (from 3 km s^{-1} to 7 km s^{-1}). The volume of highly shocked materials, classified as ≥S3, will be limited to the immediate vicinity of the impact point, and form a thin high-temperature layer at the surface of the growing crater[10]. The generation of high-temperature gas due to energy localization will lead to pulverization and explosive dispersal of the thin, high-temperature, highly shocked material layer. Highly shocked particles would hence be accelerated into space due to the ram pressure from the expanding CO and CO_2 gases. The internal energy of impact-generated vapor is converted into kinetic energy of a spherically expanding gas flow directed into space[39]. We can estimate the mass escaping from the host body M_{esc} due to the explosion by energy conservation as follows:

$$M_{vap}C_V T = \frac{1}{2} M_{esc} {v_{esc}}^2 \quad (1)$$

where M_{vap}, C_v, T, and v_{esc} are the total vapor production defined by the experiments (see Fig. 3), the isochoric specific heat of the major gas species, the temperature of the gas generated by the local energy concentration, and the escape velocity from the host body, respectively. Our experiments show M_{vap} normalized by the projectile mass is described as a power law of v_{imp}; hence, we obtain

$$\frac{M_{esc}}{M_{proj}} = 2C_V T {v_{esc}}^{-2} \alpha {v_{imp}}^{\beta}, \quad (2)$$

where M_{proj} is the projectile mass, and α, β are fitting constants to the experimental results (Supplementary Note S7, Supplementary Table S2). Figure 6 shows M_{esc} normalized by M_{proj} as a function of v_{imp}. The C_v values of CO and CO_2 were taken from the NIST–JANAF thermochemical table[40]. Kurosawa et al. (2021)[10] conducted a series of impact experiments with a CI chondrite simulant, which includes phyllosilicates, magnetite, sulfides, and organics, and measured the generated gases with the same method used in this study. The major gas was CO_2 regardless of impact velocity as well as the Fe–O–C targets used in this study. The data of the CI chondrite simulant can be also used to investigate the escaping mass from the parent bodies of hydrous CCs. Further details are described in the Methods section. Since the escaping materials are pulverized, they should be removed from the Solar system due to the interaction with the solar wind, which has been known as Pointing–Robertson effect[41], within a very short time with respect to the history of the Solar system.

To explore the efficiency of dispersal of shocked materials as a function of parent body size we consider two cases where impact occurs on a typical carbonaceous asteroid with a diameter of 100 km[42] and the asteroid (1) Ceres. To serve as a reference, we define the shocked mass M_{sh} as material that would be classified as ≥S3 (> 15 GPa). We estimate M_{sh} (also normalized by M_{proj}) by considering a vertical impact of nonporous basalt projectiles on basalt plates[43], which is also plotted in Fig. 6 as a black dashed line. The basalt line can be considered an upper limit of the shocked mass classified to ≥S3 for typical collisions between rocky bodies because it assumes vertical impact and neglects porosity. The comparison between M_{esc} and M_{sh} shows that for typical 100-km diameter carbonaceous asteroids highly shocked rocks are efficiently ejected to space. In contrast, rocks of the same shock state would be retained on the dwarf planet (1) Ceres, which is the largest known body in the asteroid belt, due to the stronger surface gravity.

Some primitive ordinary chondrites that are classified as petrologic type 3 also contain carbon up to 0.6 wt.%[44]. This carbon content does not differ substantially from the values of CO and CV chondrites[29]. According to extensive observations of the shock stage classification of ordinary chondrites[4], the degree of shock metamorphism depends on petrologic type, and highly shocked ordinary chondrites of petrologic type 3 are relatively rare. The variation in the

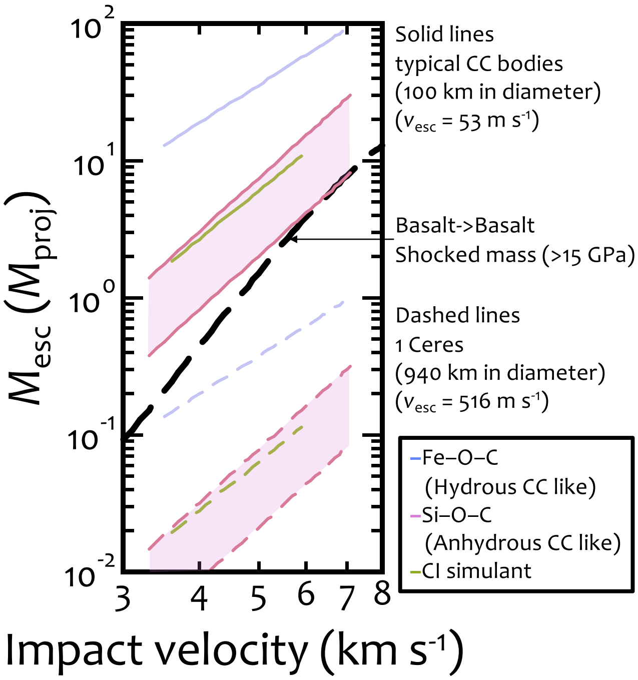

Fig. 6 | Escaping mass from carbonaceous asteroids. The graph shows the mass escaping from the host bodies M_{esc} as a function of impact velocity. The colored lines are calculated with the Eq. (2). The upper and lower lines of the Si–O–C correspond to the carbon content of 4 wt.% and 0.45 wt.%. The latter carbon content is an average of CO chondrites[29]. The upper line was obtained the experimental results and the Eq. (2). We converted the upper line to the lower one with the dependence of the carbon content on the total vapor production (Supplementary Note S2 and Fig. S2). The diameter of the host bodies and the escape velocities from their surface are indicated on the right side of the graph. The mass experiencing the compression higher than 15 GPa M_{sh} in the case of the collision between two basaltic bodies[43] is shown as the black dashed line. We also show the results for CI chondrite simulant as the green line based on the previous result[10] (See "Methods").

number fraction of meteorites with different shock stages as a function of petrologic type therefore also supports our hypothesis.

Methods

Impact experiments

We used a two-stage light gas gun at the Planetary Exploration Research Center of Chiba Institute of Technology, Japan[45]. Helium and hydrogen gases were used for projectile acceleration. An Al_2O_3 sphere with a diameter of 2 mm was used as a projectile. A nylon-slit sabot[46] was used to accelerate the projectile.

We used a quadrupole mass spectrometer (QMS, Pfeiffer Vacuum, Prisma plus QMG220) with a technique referred to as the two-valve method[30] to prevent contamination of mass spectra from the gases inevitably produced by the gun operation. This method allows direct measurement of impact-generated gases in a fully open system with the same geometry as natural impact events.

Target preparation

We used magnetite (Fe_3O_4) and quartz (SiO_2) powders to produce target pellets. Magnetite is the second major constituent of CI[47,48] and Ryugu particles[5] and is abundant in CM chondrites[49]. Although phyllosilicate is the most abundant component in hydrous chondrites[47] and Ryugu particles[5], we did not include this material in our target because a recent re-evaluation revealed that the degree of dehydration of phyllosilicates during impacts is much lower than previously expected[10]. Note that Ryugu particles, CI and CM chondrites also contain remarkable amounts of sulfides[5,48,49]. Kurosawa et al. (2021)[10] investigated the gas production and species from pellets made from a CI chondrite simulant[47], which contains sulfides. They confirmed that the impact-produced volumes of sulfur-bearing gases, such as H_2S and SO_2, were much smaller than carbon-bearing ones. Thus, we did not consider any sulfides in our samples in this study. Quartz was chosen as an analog of the silicates in the matrices of CO and CV chondrites, which are anhydrous carbonaceous chondrites, although silica is not abundant in any chondrites in general. However, the difference between silica and relevant silicates, such as olivine, pyroxene, and feldspar, does not substantially affect our experiment because of the similarity of their physical and thermoelastic properties, resulting in similar shock responses to quartz. The thermochemical behavior of quartz at high temperatures is also similar to that of olivine (Supplementary Note S5 and Fig. S6). Graphite and ^{13}C amorphous carbon powders were chosen as the simplest insoluble organic materials (IOMs) because IOMs account for the majority of the total organic carbon in both Ryugu and CCs[50]. Homogeneous powder reagents of magnetite, quartz, graphite and ^{13}C amorphous carbon with a stable quality are also easy to obtain. This allows us to conduct systematic experiments with good reproducibility. We confirmed the identity of these reagents with X-ray powder diffraction analysis (Supplementary Note S8 and Figs. S8–S11). We excluded hydrogen from the matrix and the organics in our analogs. The presence of hydrogen does not substantially affect the carbon chemistry because water vapor is chemically stable under a wide range of temperatures and redox conditions[51]. This simplification is advantageous in mass spectrometry because it allows accurate determination of the molar ratio of CO and CO_2 of the impact vapor without the contamination of the signal by hydrocarbons.

Four types of porous pellets with a diameter of 54 mm and a length of 54 mm were made. Among them are (1) magnetite only, (2) a mixture between magnetite and carbon, (3) quartz only, and (4) a mixture of quartz and carbon. In this study, they are referred to as Fe–O, Fe–O–C, Si–O, and Si–O–C, respectively. The porosity of the pellets was adjusted to ~60% as a fiducial case, which is close to the porosity of chondrite matrices[28]. We also conducted blank experiments at the velocity ranged from 3.3 km s^{-1} to 7.1 km s^{-1} with Al6061 plates. We confirmed that the generated CO, O_2, and CO_2 detected in the mass spectrometry mainly come from the target pellets, not from various sources of contamination, such as the intrusion of the combustion gases and the desorption from the chamber wall.

Shock physics modeling

We conducted a series of numerical simulations to investigate the degree of decomposition of magnetite and quartz in the non-transparent target pellets. We used the two-dimensional version of the iSALE shock physics code, iSALE-Dellen[33–36] to model the impact experiments conducted in this study. A cylindrical coordinate system was employed. The computational domain was divided into 500 × 1500 cells in the radial and vertical directions. We also set extension zones with 200 cells on the outside of the domain. The size of the computational cells in the extension zone was enlarged as a sequence of equal ratios with an extension factor of 1.02. The projectile was divided into 50 cells per projectile radius (CPPR), which corresponds to a spatial resolution of 0.02 mm $cell^{-1}$. Impact velocities were set to the same values as the experiments. We used the Tillotson equations of state (EOS)[52] with the parameter set for Al_2O_3[53] to represent the projectile and used the ANalytical Equations Of State (ANEOS)[54] for quartz[55] and magnetite to represent the targets. The parameter set for magnetite was constructed in this study based on the shock Hugoniot data[56] and thermoelastic properties of magnetite[57,58] (See Supplementary Note S9 and Figs. S12 and S13). Lagrangian tracers were inserted into all the computational grid cells in the high-resolution zone. The time variation of entropy during the simulations was stored for each tracer. We calculated the decomposed mass of magnetite and quartz with the same method used in Kurosawa, Genda et al. (2021)[53]. Since the target pellets were made from powders, the cohesion, which is defined as yield strength at zero pressure, is expected to be much lower than consolidated rocks. Although the dry friction between particles in the target pellets contributes to the yield strength of the target pellets, it would be weakened or diminished due to temperature rise[59] caused by work done during porosity compaction and the local energy concentration. Thus, we neglected any material strength in this study. The input files used in the iSALE simulations are included in Supplementary Data 1 and 2. Note that the absence of appropriate equations of state model for the mixtures of minerals and carbon precluded shock physics modeling for the target pellets with carbon as mentioned in the main text.

Explosive dispersal

The main gas products from the Fe–O–C and the Si–O–C were CO_2 and CO, respectively. We considered only the main gas product in Fig. 6. Since isochoric specific heat C_v depends on temperature, a vapor temperature of 2000 K was taken for the Fe–O–C and the Si–O–C based on Fig. 5. The C_v values of CO and CO_2 at 2000 K are 0.996 and 1.182 kJ K^{-1} kg^{-1} [40], respectively, implying that the specific internal energy E of the generated gas reaches ~2 MJ kg^{-1}. The thermal energy is converted to kinetic energy of the gas flow directed to space. The gas flow accelerates the shocked materials within the thin high-temperature layer as mentioned in the main text. Note that we also show the results for CI chondrite simulant based on the previous result[10]. The main gas released from the CI simulant was CO_2 as well as the Fe–O–C target. A vapor temperature of 1200 K[10] and C_v of 1.092 kJ K^{-1} kg^{-1} [40] were used to calculate the line for the CI simulant in Fig. 6.

Data availability

All data supporting the figures in the main text and Supplementary Figs. can be found in Source Data. The title of each source data contains the title of the figure produced used that data. The input files related to the iSALE simulations conducted in this study can be found in Supplementary Data 1 and 2. Source data are provided with this paper.

Code availability

The iSALE shock physics code and the NASA CEA code were used in this study. The iSALE is not fully open-source, and it is distributed on a case-by-case basis to academic users in the impact community for non-commercial use only. A description of the application requirements can be found at the iSALE website (https://isale-code.github.io). Any recent stable release can be used to reproduce the data. The NASA CEA can be used via the website (https://www1.grc.nasa.gov/research-and-engineering/ceaweb/).

References

1. Marchi, S. et al. High-velocity collisions from the lunar cataclysm recorded in asteroidal meteorites. *Nat. Geosci.* **6**, 303–307 (2013).
2. Stöffler, D., Hamann, C. & Metzler, K. Shock metamorphism of planetary silicate rocks and sediments: proposal for an updated classification system. *Meteorit. Planet. Sci.* **53**, 5–49 (2018).
3. Scott, E. R. D., Keil, K. & Stöffler, D. Shock metamorphism of carbonaceous chondrites. *Geochim. Cosmochim. Acta* **56**, 4281–4293 (1992).
4. Bischoff, A., Schleiting, M. & Patzek, M. Shock stage distribution of 2280 ordinary chondrites–Can bulk chondrites with a shock stage of S6 exist as individual rocks? *Meteorit. Planet. Sci.* **54**, 2189–2202 (2019).
5. Nakamura, T. et al. Formation and evolution of carbonaceous asteroid Ryugu: direct evidence from returned samples. *Science* **379**, eabn8671 (2023).
6. Tomioka, N. et al. A history of mild shocks experimenced by the regolitj particles on hydrated asteroid Ryugu. *Nat. Astron.* **7**, 669–677 (2023).
7. Miyahara, M. et al. Microscopic slickenside as a record of weak shock metamorphism in the surface layer of asteroid Ryugu. *Meteorit. Planet. Sci.* https://doi.org/10.1111/maps.14271 (2024).
8. Noguchi, T. et al. Mineralogy and petrology of fine-grained samples recovered from the asteroid (162173) Ryugu. *Meteorit. Planet. Sci.* **59**, 1877–1906 (2024).
9. Tomeoka, K., Kiriyama, K., Nakamura, K., Yamahana, Y. & Sekine, T. Interplanetary dust from the explosive dispersal of hydrated asteroids by impacts. *Nature* **423**, 60–62 (2003).
10. Kurosawa, K. et al. Ryugu's observed volatile loss did not arise from impact heating alone. *Commun. Earth Environ.* **2**, 146 (2021).
11. Brož, M. et al. Source regions of carbonaceous meteorites and near-Earth objects. *AstronomyAstrophysics* **689**, A183 (2024).
12. Brož, M. et al. Young asteroid families as the primary source of meteorites. *Nature* **634**, 566–571 (2024).
13. Hlobik, F. & Tóth, J. Orbital evolution and possible parent asteroids of 40 instrumentally observed meteorites. *Planet. Space Sci.* **240**, 105827 (2024).
14. Marsset, M. et al. The Massalia asteroid family as the origin of ordinary L chondrites. *Nature* **634**, 561–565 (2024).
15. Noonan, J. W., Volk, K., Nesvorný, D. & Bottke, W. F. Dynamical feasibility of (3) Juno as a parent body of the H chondrites. *Icarus* **408**, 115838 (2024).
16. Eugster, O., Herzog, G. F., Marti, K., Caffee, M. W. Irradiation records, cosmic-ray exposure ages, and transfer times of meteorites. *Meteorites and the Early Solar System II*, D. S. Lauretta and H. Y. McSween Jr. (eds.), 943 p.829-851 (University of Arizona Press, 2006).
17. Righter, K. et al. Mineralogy, petrology, chronology, and exposure history of the Chelyabinsk meteorite and parent body. *Meteorit. Planet. Sci.* **50**, 1790–1819 (2015).
18. Yokoyama, T. et al. Samples returned from the asteroid Ryugu are similar to Ivuna-type carbonaceous meteorites. *Science* **379**, https://doi.org/10.1126/science.abn7850 (2023).
19. Kruijer, T. S., Kleine, T. & Borg, L. E. The great isotopic dichotomy of the early Solar System. *Nat. Astron.* **4**, 32–40 (2020).
20. Trujillo, C. A., Jewitt, D. C. & Luu, J. X. Properties of the trans-Neptunian belt: statistics from the Canada–France–Hawaii telescope survey. *Astron. J.* **122**, 457–473 (2001).
21. Bottle, W. F. et al. The collisional evolution of the primordial Kuiper belt, its destabilized population, and the Trojan Asteroids. *Planet. Sci. J.* **4**, 168 (2023).
22. Bottke, W. F., Nolan, M. C., Greenberg, R. & Kolvoord, R. A. Velocity distributions among colliding asteroids. *Icarus* **107**, 255–268 (1994).
23. de Sousa, R. R. et al. Dynamical origin of the dwarf planet Ceres. *Icarus* **379**, 114933 (2022).
24. Tsiganis, K., Gomes, R., Morbidelli, A. & Levison, H. F. Origin of the orbital architecture of the giant planets of the Solar system. *Nature* **435**, 459–461 (2005).
25. Walsh, K. J., Morbidelli, A., Raymond, S. N., O'Brien, D. P. & Mandell, A. M. A low mass for Mars from Jupiter's early gas-driven migration. *Nature* **475**, 206–209 (2011).
26. Clement, M. S., Kaib, N. A., Raymond, S. N., Chambers, J. E. & Walsh, K. J. The early instability scenario: Terrestrial planet formation during the giant planet instability, and the effect of collisional fragmentation. *Icarus* **321**, 778–790 (2019).
27. Watanabe, S. & Kikuchi, S. Asteroid Ryugu and the Hayabusa2 Mission. *Oxford Research Encyclopedia of Planetary Science*. https://oxfordre.com/planetaryscience/view/10.1093/acrefore/9780190647926.001.0001/acrefore-9780190647926-e-266 (2024).
28. Bland, P. A. et al. Pressure-temperature evolution of primordial solar system solids during impact-induced compaction. *Nat. Commun.* **5**, 5451 (2014).
29. Wasson, J. T. & Kallemeyn, G. W. Compositions of chondrites. *Philos. Trans. R. Soc. Lond. Ser. A Math. Phys. Sci.* **325**, 535–544 (1988).

30. Kurosawa, K. et al. Shock vaporization/devolatilization of evaporitic minerals, halite and gypsum, in an open system investigated by a two-stage light gas gun. *Geophys. Res. Lett.* **46**, 7258–7267 (2019).
31. Shoemaker, E. M. Interpretation of lunar craters. In Z. Kopal (Ed.), *Physics and Astronomy of the Moon* (pp. 283–359) (Academic Press, 1962).
32. Schultz, P. H. Effect of impact angle on vaporization. *J. Geophys. Res.* **100**, 21117–21135 (1996).
33. Amsden, A., Ruppel, H. & C. Hirt. SALE: A simplified ALE computer program for fluid flow at all speeds. *Los Alamos National Laboratories Report*, LA-8095:101p (1980).
34. Ivanov, B. A., Deniem, D. & Neukum, G. Implementation of dynamic strength models into 2-D hydrocodes: applications for atmospheric breakup and impact cratering. *Int. J. Impact Eng.* **20**, 411–430 (1997).
35. Wünnemann, K., Collins, G. S. & Melosh, H. J. A strain-based porosity model for use in hydrocode simulations of impacts and implications for transient crater growth in porous targets. *Icarus* **180**, 514–527 (2006).
36. Collins, G. S. et al. iSALE-Dellen manual, *Figshare*, https://doi.org/10.6084/m9.figshare.3473690.v2 (2016).
37. Davison, T. M., Collins, G. S. & Bland, P. A. Mesoscale modeling of impact compaction of primitive solar system solids. *Astrophys. J.* **821**, 68 (2016).
38. Gordon, S., & McBride, B. J. Computer program for calculation of complex chemical equilibrium compositions and applications. (p. 1311). (NASA Reference Publication, 1994).
39. Melosh, H. J. *Impact cratering: A geologic process*. pp. 68–69. (Oxford University Press, 1989).
40. Chase, M. W. *NIST-JANAF Thermochemical Tables, Fourth Edition*, Journal of Physical and Chemical Reference Data Monographs (1998).
41. Grün, E., Zook, H. A., Fechtig, H. & Giese, R. H. Collisional balance of the meteoritic complex. *Icarus* **62**, 244–272 (1985).
42. Walsh et al. Introducing the Eulalia and new Polana asteroid families: re-assessing primitive asteroid families in the inner Main Belt. *Icarus* **225**, 283–2297 (2013).
43. Ono, H. et al. Experimentally shock-induced melt veins in basalt: Improving the shock classification of eucrites. *Geophys. Res. Lett.* **50**, e2022GL101009 (2023).
44. Moore, C. B. & Lewis, C. F. Total carbon content of ordinary chondrites. *J. Geophys. Res.* **72**, 6289–6292 (1967).
45. Kurosawa, K. et al. Dynamics of hypervelocity jetting during oblique impacts of spherical projectiles investigated via ultrafast imaging. *J. Geophys. Res. Planets* **120**, 1237–1251 (2015).
46. Kawai, N., Tsurui, K., Hasegawa, S. & Sato, E. Single microparticle launching method using two-stage light gas gun for simulating hypervelocity impacts of micrometeoroids and space debris. *Rev. Sci. Instrum.* **81**, 115105 (2010).
47. Britt, D. T. et al. Simulated asteroid materials based on carbonaceous chondrite mineralogies. *Meteorit. Planet. Sci.* **54**, 2067–2082 (2019).
48. King, A. J., Schofield, P. F., Howard, K. T. & Russel, S. S. Modal mineralogy of CI and CI-like chondrites by X-ray diffraction. *Geochim. Cosmochim. Acta* **165**, 148–160 (2015).
49. Howard, K. T., Benedix, G. K., Bland, P. A. & Cressey, G. Modal mineralogy of CM chondrites by X-ray diffraction (PSD–XRD): Part 2. Degree, nature and settings of aqueous alteration. *Geochim. Cosmochim. Acta* **75**, 2735–2751 (2011).
50. Yabuta, H. et al. Macromolecular organic matter in samples of the asteroid (162173) Ryugu. *Science* **379**, eabn9057 (2023).
51. Schaefer, L. & Fegley, B. Redox states of initial atmospheres outgassed on rocky planets and planetesimals. *Astrophys. J.* **843**, 120 (2017).
52. Tillotson, J. H. Metallic equations of state for hypervelocity impact. Technical Report GA-3216 (General Atomic Report, 1962).
53. Kurosawa, K., Genda, H., Azuma, S. & Okazaki, K. The role of post-shock heating by plastic deformation during impact devolatilization of calcite ($CaCO_3$). *Geophys. Res. Lett.* **48**, e2020GL091130 (2021).
54. Thompson, S. L. & Lauson, H. S. Improvements in the Chart-D radiation hydrodynamic code III: Revised analytical equation of state, pp. *SC-RR-71 0714* pp. 119 (Sandia Laboratories, 1972).
55. Melosh, H. J. A hydrocode equation of state for SiO_2. *Meteorit. Planet. Sci.* **42**, 2079–2098 (2007).
56. Marsh, S. P. *LASL Shock Hugoniot data*. pp. 301–302. (University of California Press, 1980).
57. Hidayat, T., Shishin, D., Jak, E. & Decterov, S. A. Thermodynamic reevaluation of the Fe–O system. *Comput. Coupling Phase Diagr. Thermochemistry* **48**, 131–144 (2015).
58. Siersch, N. C., Criniti, G., Kurnosov, A., Glazyrin, K. & Antonangeli, D. Thermal equation of state of Fe_3O_4 magnetite up to 16 GPa and 1100 K. *Am. Mineral.* https://doi.org/10.2138/am–2022-8571 (2022).
59. Ohnaka, M. A shear failure strength law of rock in the brittle-plastic transition regime. *Geophys. Res. Lett.* **22**, 25–28 (1995).

Acknowledgements

This work was supported by ISAS/JAXA as a collaborative program with the Hypervelocity Impact Facility. We thank the developers of iSALE, including K. Wünnemann, B. Ivanov, J. Melosh, and D. Elbeshausen. Numerical computations and analyses were in part carried out on the general-purpose PC cluster and the analysis servers at Center for Computational Astrophysics, National Astronomical Observatory of Japan. We appreciate K. Kainuma for help with the XRD analysis. We also thank S. Watanabe for useful comments on the Introduction section. This study was supported by JSPS KAKENHI Grant JP19H00726. K.K. is supported by an Academic Research Grant Project of the Hyogo Science and Technology Association (#6077). G.S.C. and T.M.D. were supported by UK STFC grant ST/S000615/1.

Author contributions

K.K. carried out the impact experiments, analyses, and numerical simulations, and wrote the initial draft of the manuscript. K.K., G.S.C., T.M.D., and T.M. conceived the initial research idea. K.K., G.S.C., T.M.D. constructed the numerical model suites. T.O. and K.I. assisted the impact experiments. All the authors, unfortunately except for late T.M., discussed the results and their implications.

Competing interests

The authors declare no competing interests.

Additional information

Supplementary information The online version contains supplementary material available at https://doi.org/10.1038/s41467-025-58474-2.

Correspondence and requests for materials should be addressed to Kosuke Kurosawa.

Peer review information *Nature Communications* thanks Kieren Torres Howard, Boris Ivanov and the other, anonymous, reviewer(s) for their contribution to the peer review of this work. A peer review file is available.